Chemical Engineering Science 280 (2023) 119090

Contents lists available at ScienceDirect

Chemical Engineering Science

journal homepage: www.elsevier.com/locate/ces

Computational fluid dynamics simulation of the heterogeneous regime in a large-scale bubble column

Nicolò Varallo, Giorgio Besagni, Riccardo Mereu *

Politecnico di Milano, Department of Energy, Via Lambruschini 4a, 20156 Milano, Italy

ARTICLE INFO

Keywords:
Bubble column
Heterogeneous flow regime
Bubbles interactions
Lift force

ABSTRACT

Bubble columns are used in many industrial applications, but the complex fluid dynamics phenomena has limited their design and optimization processes. Computational Fluid Dynamics (*CFD*) is a promising tool to investigate the complex multi-scale flow physics characterising multiphase reactors. In this work, a *CFD* Eulerian-Eulerian modelling approach is developed to describe the hydrodynamics of a large-scale bubble column operated over a wide range of superficial gas velocities (0.0188 – 0.20 m/s). Available experimental results were used for the model validation. A drag law for oblate bubbles was considered and coupled with a drag modification function to include the effects of bubble–bubble interactions. The numerical approach was tested considering a mono-dispersed approximation and including coalescence and breakup by using a Population Balance Model (*PBM*). The role played by the lift force was investigated and, for the reactor configuration considered, it turned out to be essential in the description of the local flow properties.

1. Introduction

Bubble columns are gas–liquid reactors that find many practical applications in the chemical, biochemical, petrochemical, food, and pharmaceutical industries. They are used, for example, in the Fischer-Tropsch process for the production of liquid hydrocarbons and in the *LOPROX* process which aims to improve the biodegradability of heavily contaminated production effluents (e.g., containing organic substances, i.e., phenol) before they are transferred to the traditional biological wastewater treatment facilities (Degaleesan et al. (2001), Besagni (2021a)).

Bubble columns are an attractive solution for large industrial productions due to several advantages that include simple and compact design, high durability due to the absence of moving parts, excellent heat and mass transfer coefficients, low maintenance required and low operating costs (Shaikh and Al-Dahhan (2007), Rollbusch et al. (2015), Besagni et al. (2017)). On the other hand, although their construction and layout are very simple, the hydrodynamics of bubble columns is extremely complex, and a comprehensive understanding of their properties has yet to be fully achieved. The overall behaviour of the flow is affected by phenomena occurring at both the macro-scale (reactor-scale) and the local-scale, as many operating variables tend to influence each other.

Besagni (2021b) proposed a novel physical-based theory for the description of the fluid dynamics in large-diameter bubble columns and stated that six flow regimes can be observed by increasing the gas flow rate: (1) mono-dispersed homogeneous flow regime, (2) poly-dispersed homogeneous flow regime, (3) transition flow regime without coalescence-induced structures, (4) transition flow regime with coalescence-induced structures, (5) pseudo-heterogeneous flow regime and, (6) pure-heterogeneous flow regime (Fig. 1). Changing the system design and/or the operating modes and/or the phase properties induces a variation in the flow regime boundaries and does not influence the flow regime properties themselves.

In industrial practice, large-scale bubble columns are typically employed, equipped with gas distributors characterized by large openings, so a heterogeneous flow regime is commonly observed. This regime represents a chaotic and unsteady flow pattern, with enhanced turbulent motion, strong liquid recirculation and vigorous mixing. A wide bubble size distributions and marked radial gas holdup profiles are observed (Gourich et al. (2006)). Large bubbles generated by coalescence are characterized by a negative lift coefficient explaining the radially inward motion of bubbles, whereas small bubbles with a positive lift coefficient tend to distribute toward the vessel walls (Kulkarni (2007)). The average bubble size is governed by coalescence and breakup mechanisms, which determine the flow properties, no longer controlled by the primary bubbles generated at the sparger.

* Corresponding author.
E-mail address: riccardo.mereu@polimi.it (R. Mereu).

https://doi.org/10.1016/j.ces.2023.119090
Received 14 April 2023; Received in revised form 8 June 2023; Accepted 11 July 2023
Available online 14 July 2023

Nomenclature

Abbreviations

BIT	Bubble Induced Turbulence
BSD	Bubble Size Distribution
CFD	Computational Fluid Dynamics
CFL	Courant-Friedrichs-Lewy number
LES	Large Eddy Simulation
NDF	Number Density Function
PBM	Population Balance Model
RANS	Reynolds-Averaged Navier Stokes
RSM	Reynolds Stress Model
SMD	Suter Mean Diameter

Non dimensional parameters

$Eo = \frac{g(\rho_L-\rho_G)d_{eq}^2}{\sigma}$	Eötvös number. [-]
$Fr = \frac{u_b^2}{gd_{eq}}$	Froude number. [-]
$Mo = \frac{g(\rho_L-\rho_G)\mu_L^4}{\rho_L^2\sigma^3}$	Morton number. [-]
$Re_b = \frac{\rho_L u_{rel} d_{eq}}{\mu_L}$	Reynolds number. [-]
$We = \frac{d_{eq}u_b^2\rho_L}{\sigma}$	Weber number. [-]

Symbols

D_H	Column hydraulic diameter. [m]
D_H^*	Dimensionless column diameter. [-]
C_D	Drag coefficient. [-]
C_L	Lift coefficient. [-]
d_b	Bubble diameter. [mm]
d_{eq}	Equivalent bubble diameter. [mm]
E	Bubble aspect ratio. [-]
$\vec{g}$	Gravity acceleration. [ms^{-2}]
$g(L)$	Breakage frequency. [s^{-1}]
h	Swarm factor. [-]
$h(L_1,L_2)$	Collision frequency. [m^3s^{-1}]
H_0	Initial liquid height. [m]
H_d	Aerated liquid height. [m]
k	Turbulent kinetic energy. [m^2s^{-2}]
P	Pressure. [Pa]
U	Superficial velocity. [ms^{-1}]
u_b	Bubble rise velocity. [ms^{-1}]
u_{rel}	Gas-liquid relative velocity. [ms^{-1}]

Greek letters

α_G	Local gas volume fraction. [-]
β	Daughter distribution function. [-]
Δt	Time step size. [s]
ε_G	Global gas holdup. [-]
ε	Turbulent dissipation rate. [m^2s^{-3}]
$\lambda(L_1,L_2)$	Coalescence efficiency. [-]
μ	Dynamic viscosity. [$kgm^{-1}s^{-1}$]
μ_t	Turbulent viscosity. [m^2s^{-1}]
ω	Specific dissipation rate. [s^{-1}]
ρ	Density. [kgm^{-3}]
σ	Surface tension. [Nm^{-1}]
$\bar{\tau}$	Viscous stress tensor. [$kgm^{-1}s^{-2}$]

Subscripts

G	Gas phase
L	Liquid phase
k	k-th phase

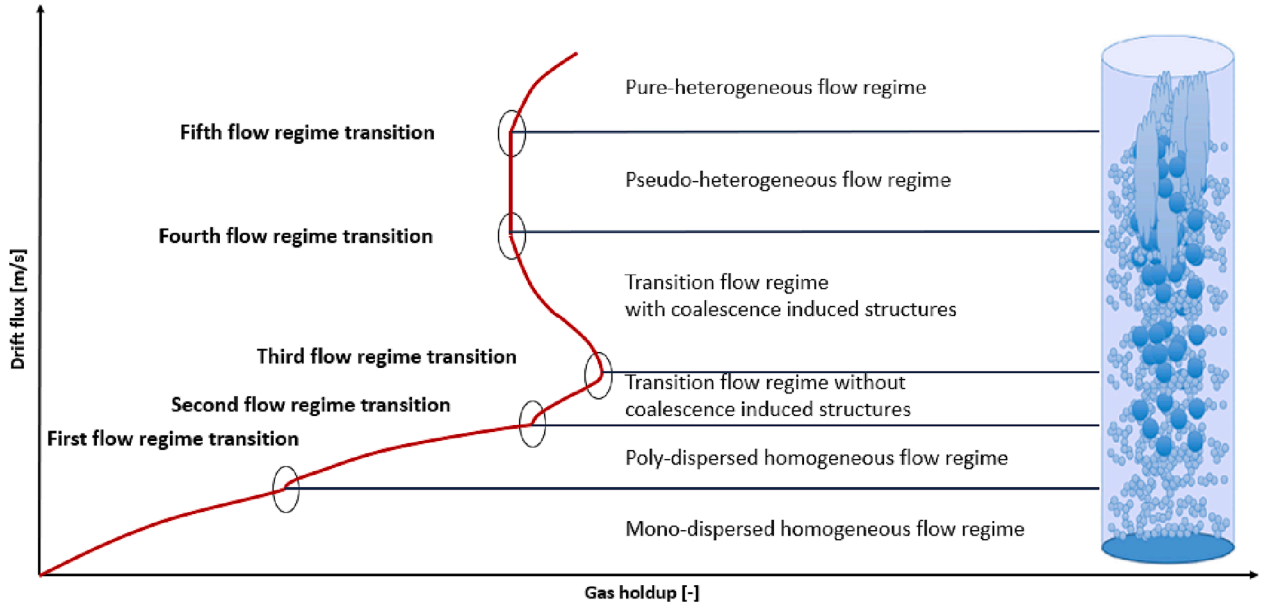

Fig. 1. Flow regimes and flow regime transitions in a large-diameter bubble column (Besagni, 2021). The drift flux is defined as the volumetric flux of either components relative to a surface moving at volumetric average velocity.

The properties of the heterogeneous flow regime make its description even more challenging (Montoya et al. (2016), Gemello et al. (2018a), Gemello et al. (2018b)). The recent increase in interest in Computational Fluid Dynamics (*CFD*) spurred substantial research efforts in determining numerical models that can obtain reasonably accurate predictions with limited computational time, thus overcoming the limitations of traditional empirical methods. Despite being a promising tool, fully predictive *CFD* models for bubble columns still need to be

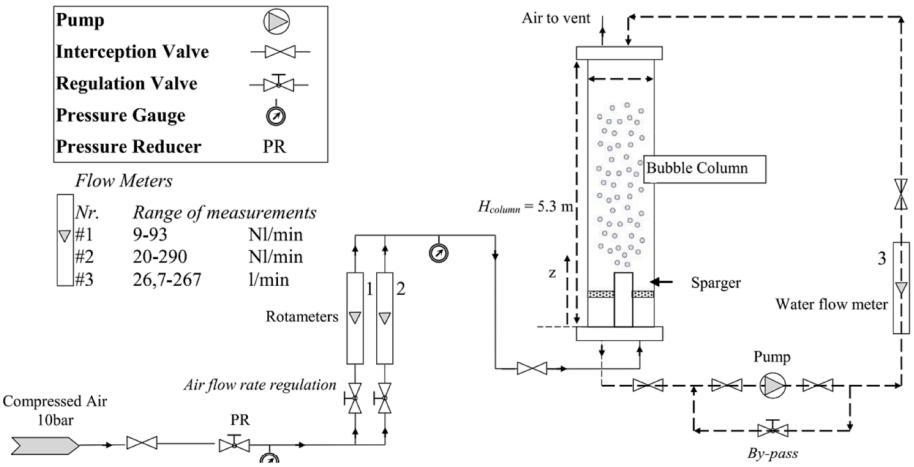

Fig. 2. Plant scheme of the experimental setup (from Besagni and Inzoli (2016)).

developed due to the lack of flow physics knowledge. Consequently, the successful use of *CFD* models still needs exhaustive experimental and numerical investigation.

The Eulerian-Eulerian multi-fluid method is the most common approach for simulating bubble columns operating with high gas volume fractions. It describes continuous and dispersed phases as interpenetrating continua and relies on ensemble averaging of the multiphase Navier-Stokes equations (Guédon et al. (2017)). This averaging procedure calls for additional closure relations that quantify the momentum transfer between the phases (Rzehak et al. (2017)).

The accuracy and reliability of the predicted results heavily depend on the selection of the closure models, on the modelling of coalescence, and breakup phenomena and on the modelling of turbulence. The literature review proposed in the following focuses on these three aspects.

Concerning the closure relations for the momentum transfer between the phases, it is admitted that the drag force gives the main contribution to the inter-phase momentum transfer (Tabib et al. (2008)). Several correlations were reported in the literature to express the drag coefficient, C_D, of a single bubble rising through an infinite liquid medium (Schiller and Naumann (1935), Grace et al. (1976), Clift et al. (1978), Ishii and Zuber (1979), Tomiyama (1998), Zhang et al. (2006)). For high volume fractions, the drag law for isolated bubble should be corrected by means of a swarm factor, which is a drag modification function that accounts for bubble–bubble interactions (McClure et al. (2014), Gemello et al. (2018a)). Among the available models, the one by Gemello et al. (2018a) appears to be the most accurate, even if it requires tuning against experimental data. Validation of swarm factors and other non-drag forces (i.e., lift, wall lubrication, turbulent dispersion, virtual mass) is still a debatable topic. In particular, the role of the lift force is controversial, as different authors found that it can be either fundamental or negligible in determining the accuracy of the results. Elena Díaz et al. (2009) (rectangular bubble column; 0.04 m width, 0.20 m length; $0.0024 \leq U_G \leq 0.021$ m/s) observed that including the lift force in the simulation did not improve the results. Similarly, Gemello et al. (2018a) (cylindrical bubble columns; $D_H = 0.4 - 1,3$ m; $0.03 \leq U_G \leq 0.35$ m/s) reported an excellent match with their experimental data even without modelling the lift coefficient. Ziegenhein et al. (2013) (cylindrical bubble column; $D_H = 0.288$ m; $U_G = 1$ cm/s) studied the effects of the interfacial forces on the hydrodynamics of a cylindrical bubble column with a fixed poly-dispersed approach. They observed that the experimental data were better predicted for high superficial gas velocities neglecting the non-drag forces. On the contrary, the lift force was fundamental to obtain satisfactory results at low superficial gas velocities. Hosseini et al. (2020) (cylindrical bubble column; $D_H = 0.24$ m; $0.0037 \leq U_G \leq 0.02$), investigated the"pseudo-homogeneous" flow regime using a bi-dispersed approach and concluded that the use of the Ziegenhein et al. (2018) lift model leads to a better prediction of the radial gas volume fraction profiles and global gas holdup.

Concerning the coalescence and breakup phenomena, they determine the local Bubble Size Distribution (*BSD*), which is essential as all interfacial forces depend on the bubble diameter. Coalescence and breakup modelling can be included by coupling the *CFD* model with a Population Balance Model (*PBM*). Recently, Gemello et al. (2019) (cylindrical bubble column; $D_H = 0.4$ m; $0.03 \leq U_G \leq 0.35$ m/s) found a set of kernels that appears to be the best choice for bubble columns operating in the heterogeneous regime. Augier et al. (2021) (cylindrical bubble column; $D_H = 0.4$ m; $0.03 \leq U_G \leq 0.35$ m/s) found the same conclusion after a screening process of 60 possible combinations of coalescence and breakage models available in literature.

Concerning turbulence, it influences the local distribution of the dispersed phase and has a crucial role in determining coalescence and breakup processes, making its modelling a fundamental aspect. Many authors have investigated the performance of different turbulence models. Deen (2001) (square bubble column; 0.15 m width, 0.15 m length; $U_G = 0.0049$ m/s) compared *RANS* and *LES* methods and demonstrated that the *RANS* approach overestimates the gas and liquid velocity profiles, while *LES* reported a better agreement with the experimental data. Ekambara and Dhotre (2010) (cylindrical bubble column; $D_H = 0.3$ m; $U_G = 0.02$ m/s) compared $k-\varepsilon$, $k-\omega$, *RSM* and *LES* models and found that both *RSM* and *LES* provided more realistic predictions near the sparger, where the flow is more anisotropic. Though, all models predicted comparable time-averaged quantities. Silva et al. (2012) (cylindrical bubble column; $D_H = 0.162$ m; $0.02 \leq U_G \leq 0.08$ m/s) studied the applicability of $k-\varepsilon$ and *RSM* turbulence model in the heterogeneous flow regime and found that both could provide a good quantitative description of gas holdup and velocity profiles in the fully developed region. Colombo and Fairweather (2015) (cylindrical bubble columns; $0.025 \leq D_H \leq 0.06$ m; $0.02 \leq U_G \leq 0.436$ m/s) applied *RSM* and $k-\varepsilon$ models combined with Bubble Induced Turbulence (*BIT*) source terms to represent the gas volume fraction and axial liquid velocity radial profile in both upward and downward air–water flows. They concluded that the anisotropy of the turbulence field was well reproduced with the *RSM*, which gave accurate predictions of the stream-wise and the wall-normal rout mean square of velocity fluctuations. However, a close agreement was found between the two methods.

Although some authors proposed their own set of closure models, comprehensive guidelines concerning the heterogeneous regime still need to be revised, as most of the research has focused on column operation at low gas velocities. For example, Guédon et al. (2017) developed a model that provided good results for the homogeneous

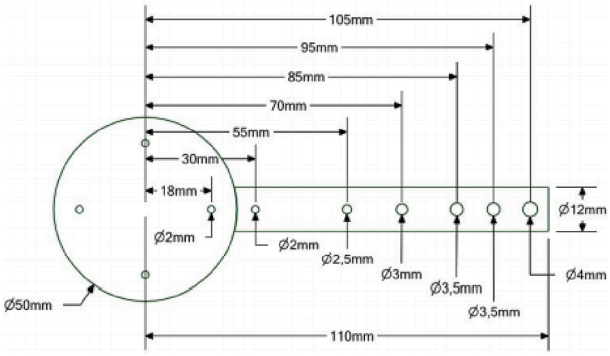

Fig. 3. Spider sparger geometrical configuration.

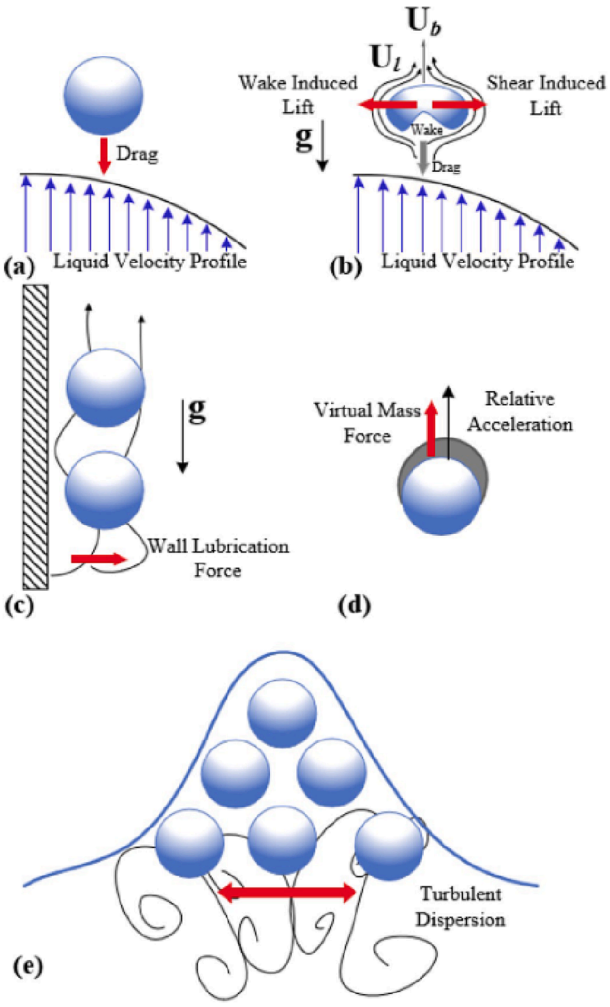

Fig. 4. Schematic of interphase forces acting on a bubble: (a) Drag, (b) Lift, (c) Wall lubrication force, (d) Virtual mass force, (e) Turbulent dispersion force (Khan et al. (2020)).

regime but proved inaccurate when applied to the heterogeneous one.

Considering the gaps present in the current numerical modelling of bubble columns, this work attempts to develop a *CFD* methodology that can describe the fluid dynamics of a large-scale reactor operated in the heterogeneous regime, with the superficial gas velocity ranging from 0.0188 m/s to 0.20 m/s.

Firstly, a fixed bubble size assumption is adopted modelling only the drag force corrected with a swarm factor. Then, improvements in the use of a *PBM* will be quantified. The role of the lift force will be examined by adding a proper lift coefficient formulation and checking the radial distribution of local properties.

This paper is structured as follows. In Section 2 the experimental set-up and dataset are presented, in Section 3 the numerical approach is discussed and the physical model is detailed, in Section 4 the numerical predictions are compared with experiments. Finally, conclusions are drawn and future studies are proposed.

2. The experimental data

The experimental set-up of Besagni and Inzoli (2016) (Fig. 2) was used as a reference for this work. The experimental facility consist of a non-pressurized vertical pipe made of Plexiglas with height $h_C = 5.3$ m and inner diameter of$D_C = 0.24$ m. A pressure reducer controls the pressure upstream the rotameters (1) and (2), used to measure the gas flow rate (accuracy 2 % f.s.v., E5-2600/h, manufactured by ASA, Italy). A pump (manufactured by DAB), controlled by a bypass valve, provides water recirculation, and a rotameter (3) measures the liquid flow rate (accuracy 1.5 % f.s.v., G6-3100/39 manufactured by ASA, Italy). The air distributor is a spider sparger with 6 arms and 40 holes of diameter ranging between 2 mm and 4 mm (Fig. 3). The liquid and gas temperatures were kept constant at room temperature (22±1 °C), and the value of gas density (used to calculate the superficial gas velocity) refers to the operating conditions at the column mid-point.

Measurement of the bed expansion allowed the evaluation of the gas holdup. The procedure involves measuring the location (height) of the liquid free surface before and after the aeration.

$$\varepsilon_G = \frac{H_d - H_0}{H_d} \tag{1}$$

Where H_0 is the initial liquid height and H_d is the height of the liquid free surface after the aeration.

The local flow properties were measured using a double-fiber optical probe (manufactured by RBI). The optical probe is inserted, via an access port, in the flow at heigh of 0.7 m and 1.9 m from the sparger. The first probe measures the near sparger flow characteristics, the latter is positioned in the region of full development flow, and the measurements refer to the hydrodynamic condition of all the other points located at higher axial positions.

Bubble size distribution is obtained by image analysis. The photos were taken using a NIKON camera (f/3.5, 1/1600 s, ISO400); the backlight method is employed in the experiments using a 500 W halogen lamp as the light source. Visualization sections consist of squared boxes (filled with water) around the vertical pipe designed to correct the distorted image. The resolution of each image is 4288 × 2848 pixels.

The reactor is operated in batch mode and the initial liquid height is set to 3.4 m, which is assumed to be high enough to consider the gas volume fraction independent on the initial level of the liquid free surface. Superficial gas velocity can be varied in the range between 0.0037 m/ s and 0.2 m/s.

Note that the column also respects all the scale-up criteria indicated in the paper of Wilkinson et al. (1992). For its geometrical characteristics, the column is classified as a large-scale facility, following the definition of Kataoka and Ishii (1987), based on the dimensionless diameter, D_H^*.

$$D_H^* = \frac{D_H}{\sqrt{\frac{\sigma}{g}(\rho_L - \rho_g)}} \geq 52 \tag{2}$$

3. Numerical modelling

3.1. Governing equations

In the Eulerian-Eulerian framework the different phases are treated mathematically as interpenetrating continua. Conservation equations

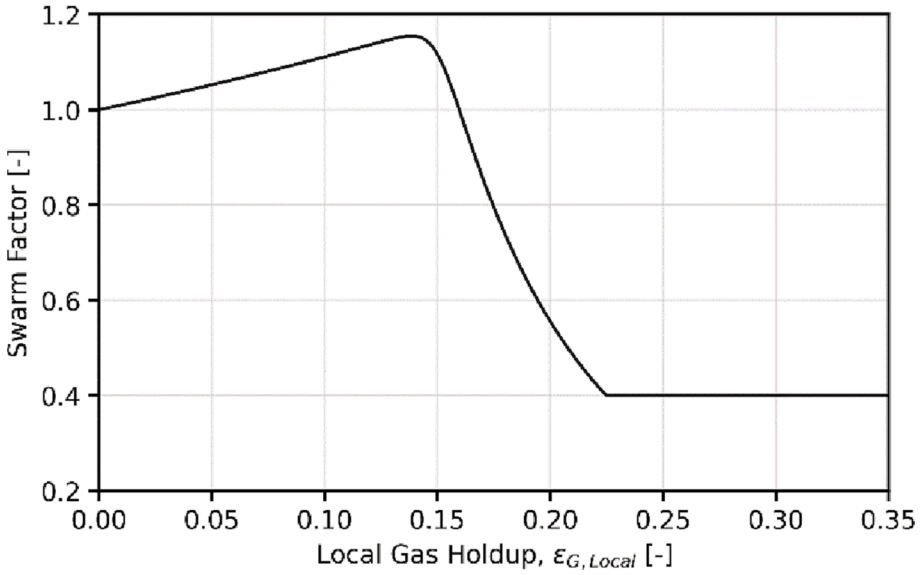

Fig. 5. Swarm factor as a function of the local gas holdup.

are evaluated for each phase, defining a set of governing relations that is solved at each computational cell. Considering an isothermal flow with no mass transfer, the continuity equation for the *k*-th phase is:

$$\frac{\partial}{\partial t}(\alpha_k \rho_k) + \nabla \bullet (\alpha_k \rho_k \vec{u}_k) = 0 \tag{3}$$

Where $\vec{u}_k$ is the velocity vector of phase *k* and α_k is the phasic volume fraction. The momentum balance for *k*-th phase reads as follows.

$$\frac{\partial}{\partial t}\left(\alpha_k \rho_k \vec{u}_k\right) + \nabla \bullet \left(\alpha_k \rho_k \vec{u}_k \vec{u}_k\right) = -\alpha_k \nabla P + \nabla \bullet (\alpha_k \bar{\tau}_k) + \alpha_k \rho_k \vec{g} + \vec{M}_k \tag{4}$$

Where $\vec{g}$ is the gravity acceleration, *P* is the common pressure field shared by all phases, and $\bar{\tau}_k$ is the shear-stress tensor for the *k*-th phase. The last term appearing on the right-hand side of Equation (4) includes all the interaction forces exchanged between the phases. It is given by the sum of the following inter-phase mechanisms: drag, lift, turbulent dispersion, wall lubrication, and virtual mass (Fig. 4).

$$\vec{M}_k = \vec{F}_D + \vec{F}_L + \vec{F}_{TD} + \vec{F}_{WL} + \vec{F}_{VM} \tag{5}$$

3.2. Interfacial forces

Interfacial momentum forces are typically added as source terms in the momentum equation and can be classified into drag and non-drag forces. The drag force gives the most important contribution to the momentum transfer between phases, but the other forces (especially the lift force) may still have an impact in determining the local flow properties distribution. Virtual mass and wall lubrication have no significant contribution to the momentum transfer in bubble columns, so they have been neglected in this work. This allows also to simplify the CFD model, increasing stability and reducing the volume of calculations. Moreover, the turbulent dispersion force was not included directly because its effects are comprised in the definition of the swarm factor. Only the drag and lift force are implemented and discussed in the present analysis.

3.2.1. Drag force

The drag force takes into account the resistance force that opposes to the bubble motion relative to the surrounding liquid (Rzehak et al. (2017)). It is always applied in the opposite direction to the bubble motion and its formulation includes local quantities like the relative gas–liquid velocity, bubble diameter, and gas volume fraction.

$$\vec{F}_D = -\frac{3}{4 d_b} C_D \rho_L \alpha_G (1-\alpha_G) |\vec{u}_G - \vec{u}_L| (\vec{u}_G - \vec{u}_L) \tag{6}$$

C_D is the actual drag coefficient and can be evaluated in the ideal case of an isolated bubble with suitable correlations for different flow and bubble shape regimes. The drag law of Tomiyama (1998) was used in this work.

$$C_D^{\infty} = \max\left\{\min\left[\frac{24}{Re_b}\left(1 + 0.15 Re_b^{0.687}\right), \frac{72}{Re_b}\right], \frac{8}{3}\frac{Eo}{Eo+4}\right\} \tag{7}$$

Equation (7) shows the dependence of the drag coefficient on two important dimensionless parameters, the Reynolds number, Re_b, and the Eötvös number, *Eo*. It is particularly suitable for oblate and deformable bubbles and is also valid for partially contaminated systems (Gemello et al. (2018a)).

3.2.2. Swarm factor

In the case of high gas volume fraction, bubbles are very close to each other, so a crowding effect is observed, for which bubbles travel through the column in swarms. In these clusters, the bubble boundary layers interact, modifying the interphase momentum exchange and, above all, the drag force.

To quantify this change in the drag force a correction function is defined, termed swarm factor, that is calculated as the ratio between the actual drag coefficient and the ideal drag coefficient for an isolated bubble.

$$h = \frac{C_D}{C_D^{\infty}} \tag{8}$$

Recently, Gemello et al. (2018a) proposed a correlation that gives good results when applied to air–water bubble columns in the heterogeneous regime. They corrected the model of Simonnet et al. (2008), which was validated only for gas fractions lower than 30%, by including a minimum constant value, $h_{\min}$.

$$h = \max\left\{(1-\alpha_G)\left[(1-\alpha_G)^{25} + \left(4.8\frac{\alpha_G}{1-\alpha_G}\right)^{25}\right]^{-\frac{2}{25}}, h_{\min}\right\} \tag{9}$$

$h_{\min}$ is an adjustable parameter and must be tuned to the experimental data. A sensitivity analysis on the $h_{\min}$ value was performed and it was found that $h_{\min} = 0.4$ provides the best results. Fig. 5 shows the swarm factor considered in this study.

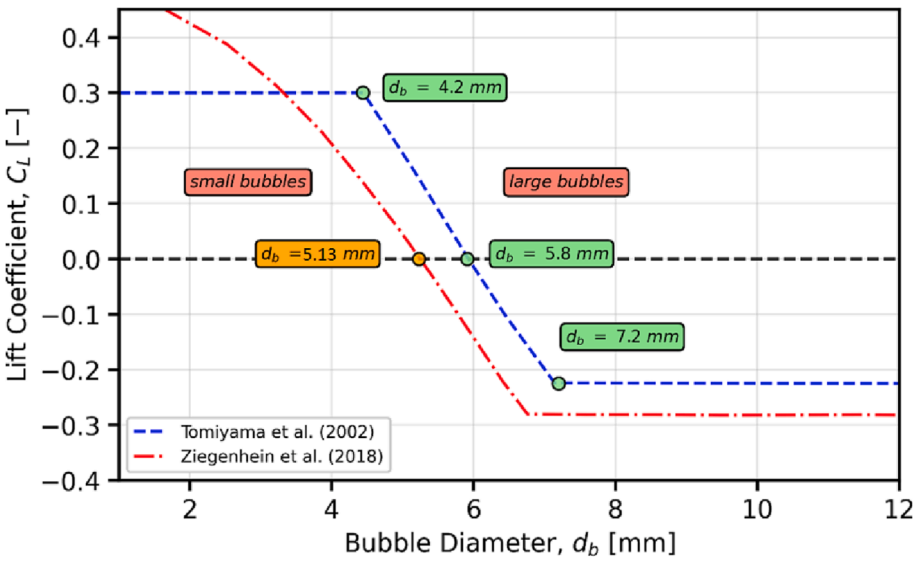

Fig. 6. Comparison between Tomiyama et al. (2002) and Ziegenhein et al. (2018) model for the lift coefficient. Note that the two models predict different values for the critical diameter in air–water systems.

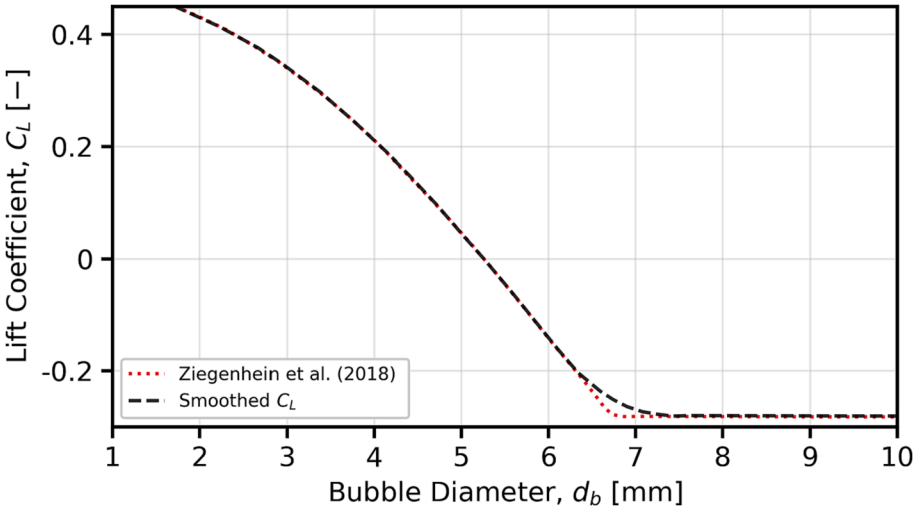

Fig. 7. Comparison between the Ziegenhein et al. (2018) lift model (dotted line) and the smoothing function proposed in Equation 16 (dashed line).

3.2.3. Lift force

The lift force is a transverse force component that acts in the direction perpendicular to the bubble motion. The momentum source term given by the lift force is calculated as following.

$$\vec{F}_L = -C_L \alpha_G \rho_L (\vec{u}_G - \vec{u}_L) \times (\nabla \times \vec{u}_L) \tag{10}$$

The lift force heavily depends on the bubble size and shape. In particular, small bubbles have a positive lift coefficient, so that the lift force acts in the direction of negative liquid velocity gradient, pushing them towards the reactor walls. Large bubbles, instead, have a negative lift coefficient and tend to move towards the column centre. The lift coefficient sign reversal occurs at a specific bubble size, referred to as critical bubble diameter, d_{crit}.

Tomiyama et al. (2002) experimentally studied the motion of an isolated air bubble rising in a vertical shear flow of glycerol-water solution (Morton number between 10^{-3} and 3×10^{-3}) and derived a model for the lift force applicable to large-scale deformable bubbles. Satisfactory results were also obtained when the model was extended to air–water systems (Morton number of 10^{-10}).

$$C_L = \begin{cases} \min[0.288\tanh(0.121 Re_b), f(Eo_\perp)] & Eo_\perp \le 4 \\ f(Eo_\perp) & 4 < Eo_\perp \le 10 \\ -0.27 & Eo_\perp > 10 \end{cases} \tag{11}$$

Where:

$$f(Eo_\perp) = 0.00105 Eo_\perp^3 - 0.0159 Eo_\perp^2 - 0.0204 Eo_\perp + 0.474 \tag{12}$$

$Eo_\perp$ is the modified Eötvös number.

$$Eo_\perp = \frac{g(\rho_L - \rho_G) d_\perp^2}{\sigma} \tag{13}$$

It is calculated considering the maximum horizontal dimension (major axis) of the bubble, $d_\perp$, which depends on the bubble aspect ratio, E. A widely used correlation to predict the bubble aspect ratio was given by Wellek et al. (1966) for contaminate flows.

$$d_\perp = d_b \left(\frac{1}{E}\right)^{1/3} = d_b \sqrt[3]{1 + 0.163 Eo^{0.757}} \tag{14}$$

With the Wellek et al. (1966) shape correlation, the Tomiyama et al. (2002) model predicts that the sign change occurs at a bubble size of 5.8

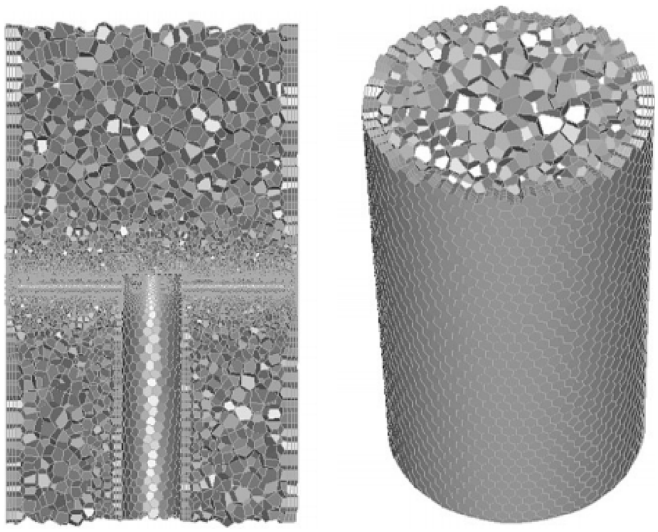

Fig. 8. 3D representations of the polyhedral mesh at two different locations: (left) Sparger region, (right) Interior region.

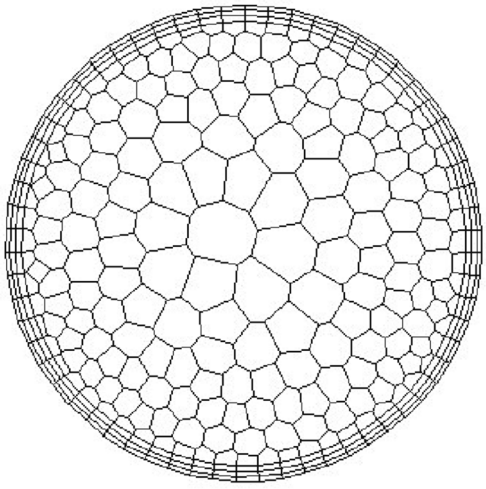

Fig. 9. Cross sectional view of the polyhedral mesh used in this work.

Table 1
Summary of the solution methods used in the CFD simulations.

Equation	Solution Method
Pressure	PRESTO!
Gradient	Least-Square Cell Based
Momentum	QUICK
Volume Fraction	QUICK
Turbulence	First-Order Upwind
Gas size bins	First-Order Upwind

mm. However, Ziegenhein and Lucas (2019) pointed out that Wellek et al. (1966) correlation is not suitable for purified air–water systems, leading to an overprediction of the major axis for an elliptic bubble. To overcome this limitation, Ziegenhein et al. (2018) suggested a quadratic fit correlation for the lift force as a function of Morton number, modified Eötvös number and bubble Reynolds number.

$$C_L = \begin{cases} 0.002Eo_\perp - 0.1Eo_\perp + 0.5 & Eo_\perp \leq 10.5 \\ -0.3295 & Eo_\perp < 10.5 \end{cases} \tag{15}$$

In the model, the correlation for the bubble major axis is modified based on experimental observation of bubble shapes in six column configurations.

$$d_\perp = d_b \sqrt[3]{1 + 0.65Eo^{0.35}} \tag{16}$$

The Ziegenhein et al. (2018) correlation results in a critical diameter of about 5.13 mm, which is lower than that obtained by the Tomiyama et al. (1998) model coupled with the Wellek et al. (1966) relation for the bubble aspect ratio. Fig. 6 shows the comparison between Tomiyama et al. (1998) and Ziegenhein et al. (2018) lift model.

The lift force modelling adds a noticeable degree of instability to the simulation, and thus certain precautions are required. To avoid possible convergence issues, the lift coefficient formulation given by Ziegenhein et al. (2018) was smoothed (Fig. 7) to prevent rapid variations in the lift coefficient with the increase in the bubble diameter. The smoothed function has the following form:

$$C_{L,\text{smooth}} = a\left(0.002Eo_\perp^2 - 0.1Eo_\perp + 0.5\right) - 0.3295(1-b) \tag{17}$$

Where the a and b coefficients are given by

$$a = \frac{1}{2} - \frac{1}{2}\tanh\left(\frac{Eo_\perp - 10.3}{1.5}\right) \tag{18}$$

$$b = \frac{1}{2} - \frac{1}{2}\tanh\left(\frac{Eo_\perp - 10.6}{1.5}\right) \tag{19}$$

3.3. Population balance model

When the information about the bubble size distribution is not available, the mono-dispersed approach cannot be implemented, and a population balance model can be used. The class method was adopted, since the Quadrature Method of Moments (*QMOM*) suffered from numerical issues that produced sets of corrupted moments which lead to a misrepresentation of the computed flow.

In the class method the continuous bubble size distribution is discretized into different size bins. The interval of bubble diameters associated with each bin is calculated with the following geometrical progression.

$$\frac{V_{i+1}}{V_i} = 2^q \tag{20}$$

Where V_i is the bubble volume of the *i-th* bin. In terms of bubble diameter:

$$\frac{d_{i+1}}{d_i} = \sqrt[3]{2^q} \tag{21}$$

The number of bins was set equal to 16 since it demonstrated to be a good compromise between accuracy and computing time. A value of 1.15 was chosen for the ratio exponent, q. In this way, by selecting the minimum diameter to be 1 mm, the maximum allowed bubble size is 54 mm.

Table 2
Air and water density, dynamic viscosity, and surface tension coefficient at the midpoint of the column.

Phase	Density [kg/m^3]	Dynamic Viscosity [kg s/m]	Surface Tension Coefficient [N/m]
Primary (Water)	997	$8.9 \cdot 10^{-4}$	–
Secondary (Air)	1.356	$1.85 \cdot 10^{-5}$	–
Air-Water	–	–	0.072

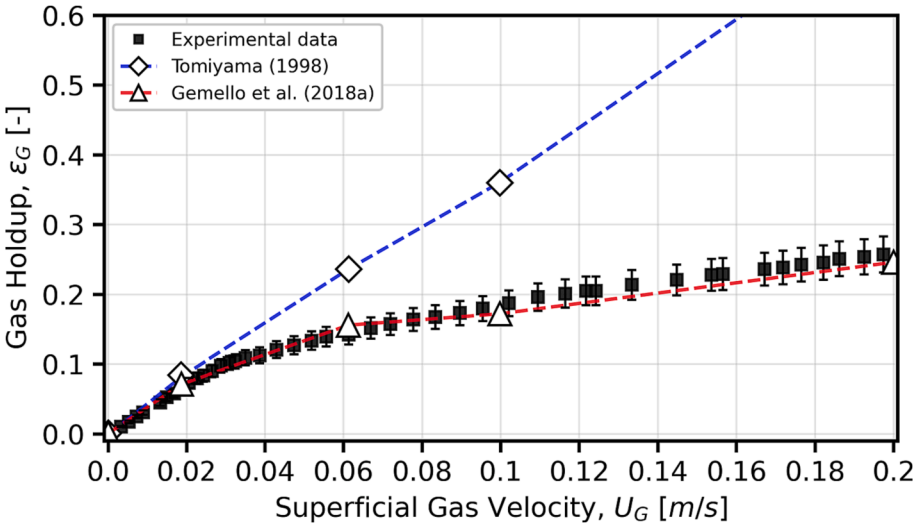

Fig. 10. Comparison between experimental data (■) and CFD simulation results using the drag law of Tomiyama (1998) (◇) and considering the modified version of the swarm factor proposed by Gemello et al. (2018a) (△). Error bars indicate a 10 % error margin with respect to the corresponding experimental value (a value commonly associated with the bed expansion technique, used for measuring the global gas holdup).

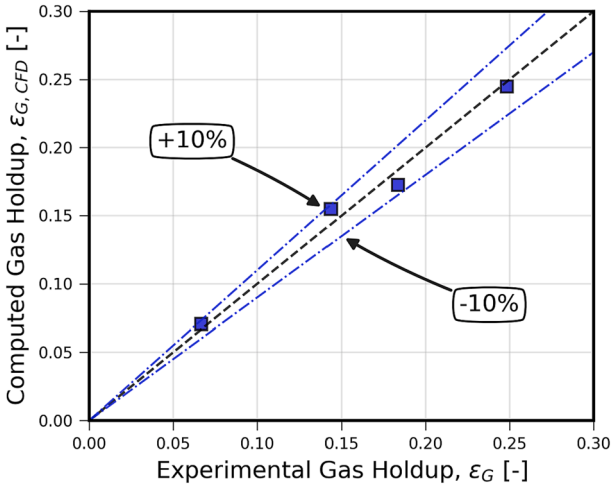

Fig. 11. Parity graph of experimental and calculated *CFD* results for the global gas holdup. The error lines indicate that the results for the simulated flow conditions fall within the ± 10% margin.

3.3.1. Bubble breakup model

The modelling of the breakage phenomena requires the definition of a breakage efficiency and of a daughter size distribution function. Indicating with L the diameter of the daughter bubble and following the study of Gemello et al. (2018) the expression for the breakage frequency adopted is based on the work of Laakkonen et al. (2006).

$$g(L) = C_3 \varepsilon^{1/3} \mathrm{erfc}\left(\sqrt{\frac{C_4\sigma}{\rho_L \varepsilon^{2/3} L^{5/3}} + \frac{C_5 \mu_L}{\sqrt{\rho_L \rho_g}\,\varepsilon^{1/3} L^{4/3}}}\right) \tag{22}$$

Three adjustable constants appear in the expression for $g(L)$. The constants C_4 and C_5 are independent on the system characteristics and are set equal to 0.04 and 0.01, respectively. The first multiplication constant C_3 contains the dependency on the physical and flow properties and was assumed equal to 4.0 $m^{-2/3}$, as suggested by Gemello et al. (2019). This value is considered valid for all bubble columns operating with air–water flows. However, the constant C_3 changes as the system properties change. For example, Petitti et al. (2013) found that $C_3 = 6$ $m^{-2/3}$ provides satisfactory results when dealing with air–water stirred tank reactors. Moreover, C_3 is expected to change when fluids other than air and water are used, and it should be tuned based on experimental data. This dependency is not investigated in this work. The daughter distribution function also considers the model of Laakkonen et al. (2006) and assumes binary breakage.

3.3.2. Bubble coalescence model

Concerning the modelling of coalescence, the relation for the collision frequency proposed by Wang et al. (2005) was adopted.

$$h(L_1, L_2) = C_6' \gamma \Pi (L_1 + L_2)^2 \sqrt{L_1^{2/3} + L_2^{2/3}}\,\varepsilon^{1/3} \tag{23}$$

The model constant C_6' should be replaced to match the experimental data for the *SMD*, and a value of 0.16 was used in this study (Gemello et al. (2019)).

As detailed in Liao and Lucas (2010), γ and Π are modification functions. Function γ accounts for reduction of the free space for bubble movement due to the volume occupied by bubbles, which causes an increase in the collision frequency.

$$\gamma = \frac{\alpha_{G,\max}}{\alpha_{G,\max} - \alpha_G} \tag{24}$$

Function Π is linked to the fact that, when bubbles are much larger than the turbulent length scale, they are not influenced by turbulence and no collisions occur. Wu et al. (1998) suggested the following expression, assuming that the bubble distance for which collisions between neighbouring bubbles take place is by the eddy with size of the same order of the bubble size.

$$\Pi = \left[1 - \exp\left(-C_\Pi \frac{\alpha_{G,\max}^{1/3} \alpha_G^{1/3}}{\alpha_{G,\max}^{1/3} - \alpha_G^{1/3}}\right)\right] \tag{25}$$

C_Π is an adjustable parameter that can be set as 3 in case of air–water systems. The critical approach velocity is selected for the coalescence efficiency with the model of Lehr et al. (2002).

$$\lambda(L_1, L_2) = \min\left(\frac{u_{\mathrm{crit}}}{u_{\mathrm{rel}}}, 1\right) \tag{6}$$

The term u_{crit} is equal to 0.08 m/s for air–water systems. The relative approach velocity is determined as:

$$u_{\mathrm{rel}} = \sqrt{2}\varepsilon^{1/3}\sqrt{L_1^{2/3} + L_2^{2/3}} \tag{27}$$

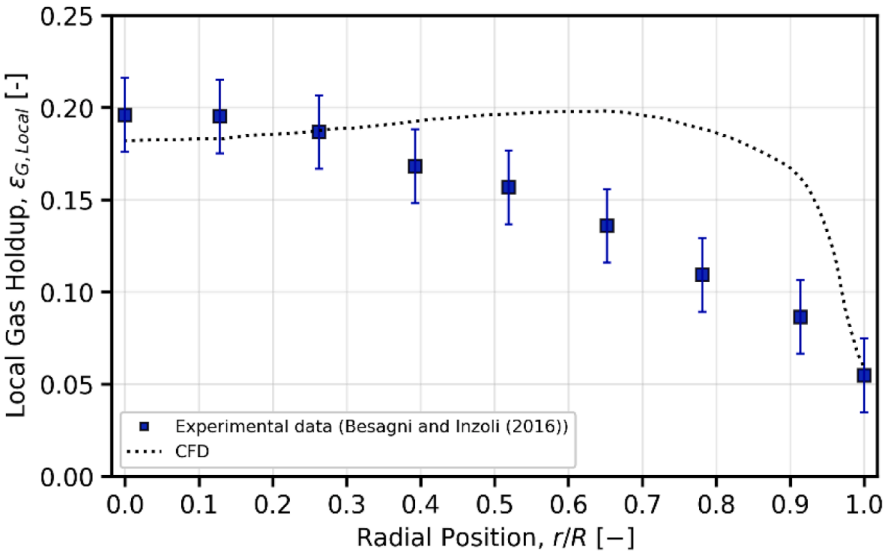

(a)

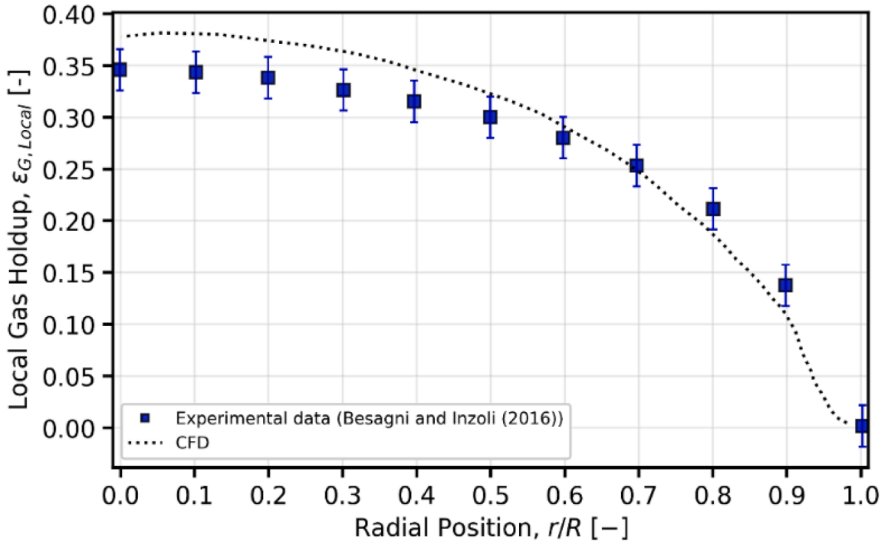

(b)

Fig. 12. Radial distribution of the local gas volume fraction determined from the *CFD* simulation at the axial position of 1.9 m from the sparger at $U_G = 0.0614$ m/s (a) and $U_G = 0.20$ m/s (b) using the mono-dispersed approach (dotted line) versus the experimental data (■). Error bars represent the standard error of the experimental data.

Where L_1 and L_2 are the sizes of the approaching bubbles, and ε is the turbulent dissipation rate.

3.4. Turbulence modelling

Due to the small density of the dispersed gas, it suffices to consider turbulence in the continuous phase (Rzehak and Krepper, 2013b). The two-equation $k-\omega$ Shear-Stress-Transport (*SST*) was implemented to estimate the Reynolds stresses and the Production Kato-Launder modification option was selected. The constants of the model follow their single phase counterparts. In the present study, Bubble Induced Turbulence (*BIT*) has been neglected.

3.5. Geometry and mesh properties

The numerical simulations were performed on a 3D unstructured polyhedral mesh. A mesh independence analysis was performed to check the dependence of the results on the cell size, and it was concluded that a

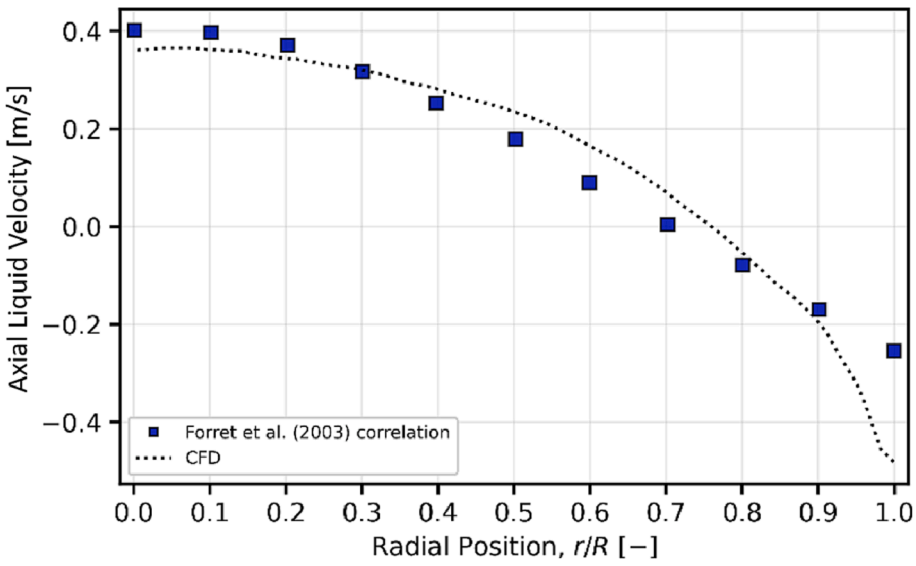

Fig. 13. Radial distribution of the local axial liquid velocity determined from the CFD simulation at axial position of 1.9 m from the sparger at $U_G = 0.0614$ m/s: (dotted line) CFD results versus (■) Forret et al. (2003) correlation.

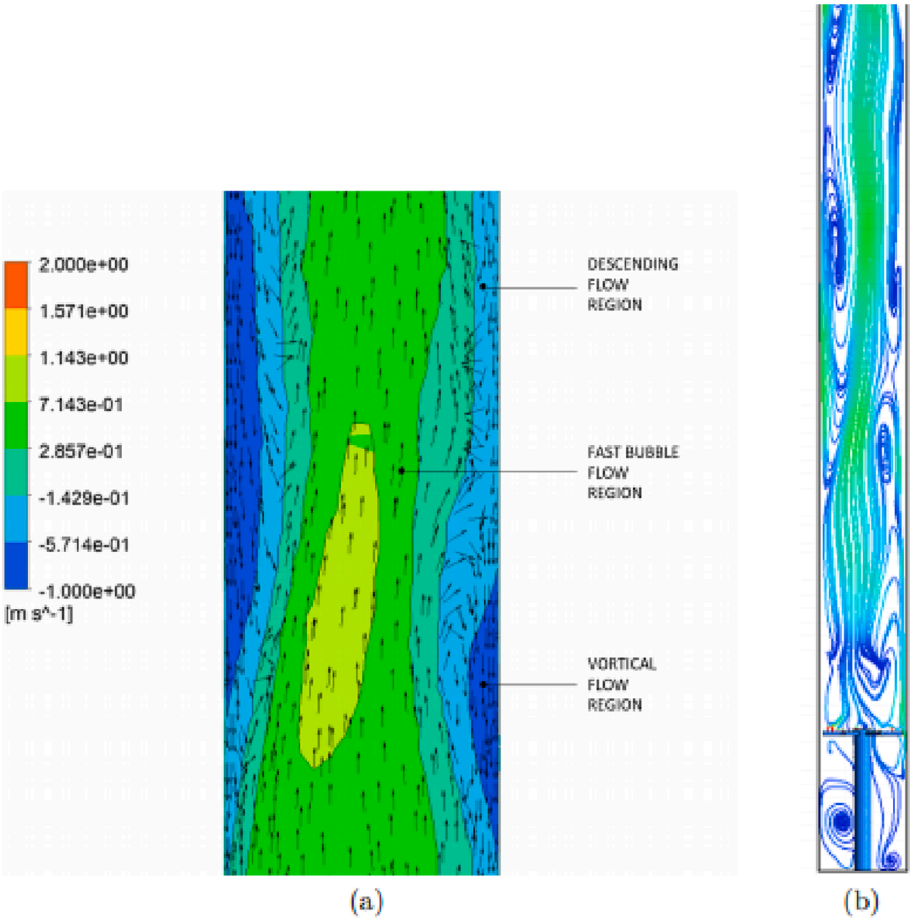

Fig. 14. Visualization of the instantaneous macro-scale flow structures over the axial plane at $U_G = 0.10$ m/s: (a) Contours of axial liquid velocity, (b) Pathlines of axial liquid velocity.

medium mesh with about 313 000 elements is sufficiently fine to ensure results that are independent on the grid size. Results of the independence analysis are shown in Appendix A. In the geometrical representation, the spider sparger was modelled with its fully 3D structure without including any simplifications in order to describe the complex flow patterns occurring at the gas inlet (Fig. 8, Fig. 9). The advantage in using polyhedral meshes is that they typically allow lower overall cell count relative to unstructured tetrahedral or hybrid meshes, possibly

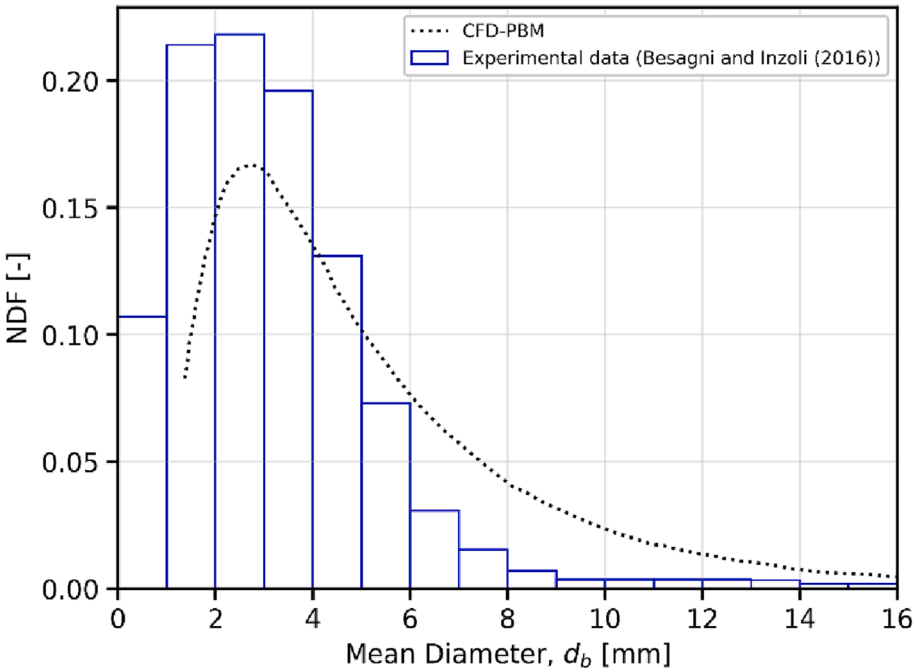

Fig. 15. Histogram representing the experimental *BSD* at $U_G = 0.0188$ m/s, compared with *BSD* predicted by the *CFD* model adopting the *PBM* (dotted line).

Table 3
CFD results for the global gas holdup obtained using the swarm factor and the *PBM*, compared to the experimental values. In brackets, the relative error e [%] between the numerical result and the experimental value, $e = |\varepsilon_{G,EXP} - \varepsilon_{G,CFD}|/\varepsilon_{G,EXP}$.

Superficial Gas Velocity [m/s]	Global Gas Holdup Swarm Factor [%]	Global Gas Holdup PBM [%]	Experimental Value [%]
0.0188	7.1 (7.6)	7.1 (7.6)	6.6
0.0614	15.4 (7.2)	15.7 (9.3)	14.4
0.10	17.2 (6.6)	17.0 (7.7)	18.4
0.20	24.4 (4.5)	24.9 (2.6)	25.6

saving some computational expense. The computational grid was refined near the wall (where three prism layers were adopted) to capture the boundary layer gradients, and near the sparger, due to the presence of small geometrical details and complex flow field. During the mesh generation process, good grid quality was also ensured, as poor quality discretization can either cause convergence difficulties and inaccurate physics description. The quality parameter values are in the optimal range. The majority of the cells have a very high orthogonal quality value, between 0.8 and 0.9998, and just few cells reach lower quality. In particular, some cells near the sparger openings and near the outer edge

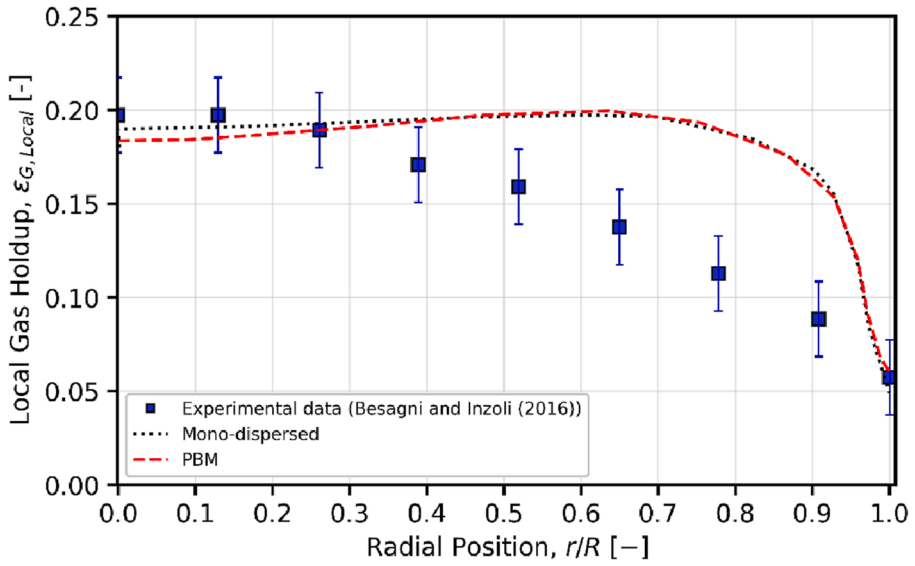

Fig. 16. Comparison of the *CFD* results for the radial profile of local gas holdup at the axial position of 1.9 m from the sparger at $U_G = 0.0614$ m/s using the mono-dispersed approach (dotted line) and the *PBM* (dashed line) versus the experimental data (■). Error bars represent the standard error of the experimental data.

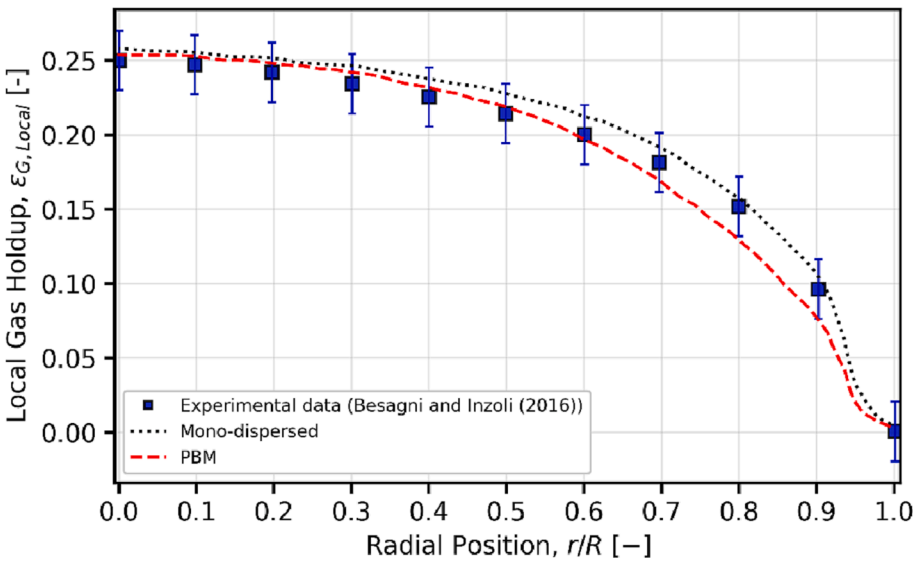

Fig. 17. Comparison of the *CFD* results for the radial profile of local gas holdup at the axial position of 1.9 m from the sparger at $U_G = 0.10$ m/s using the mono-dispersed approach (dotted line) and the *PBM* (dashed line) versus the experimental data. Error bars represent the standard error of the experimental data (■).

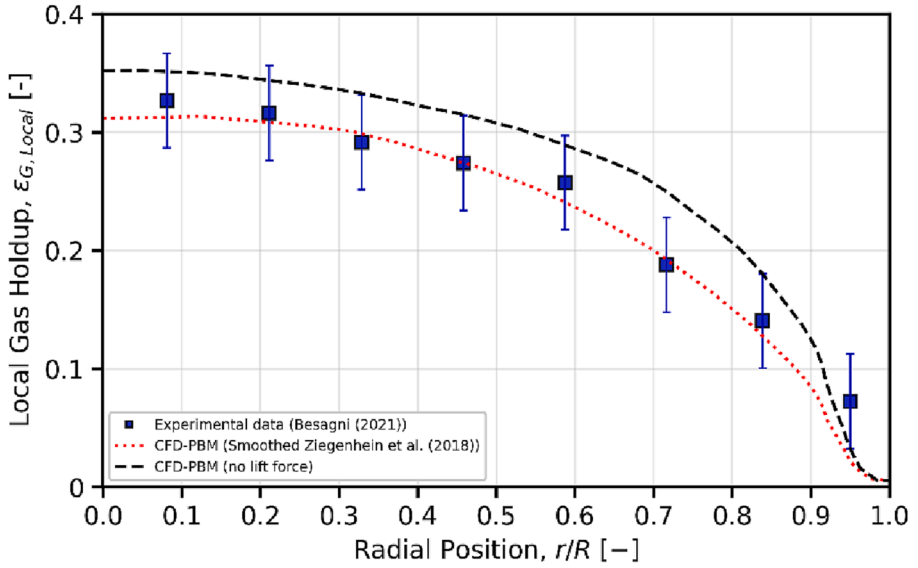

Fig. 18. Comparison of the *CFD* results for the radial profile of local gas holdup at the axial position of 1.9 m from the sparger at $U_G = 0.20$ m/s using the *PBM* with lift force (dotted line) and the *PBM* without lift force (dashed line) versus the experimental data (■). Error bars represent the standard error of the experimental data.

of the sparger arms reach the minimum quality level, found at 0.45. The maximum skewness is 0.55 and the maximum aspect ratio is 22.8, which are quite high but refer only to a limited amount of cells located near the sparger. The overall quality of the mesh can be considered satisfactory and no degenerate cells are found when performing the mesh check.

3.6. Numerical settings and boundary conditions

Transient 3D simulations were performed on commercial software ANSYS Fluent 2021 R2 using the Eulerian – Eulerian approach over a time interval of 120 s. Results were averaged for the last 100 s of flow time, to ensure that they are independent on the initial transient (from the physical point of view, the initial transient decays after 10–15 s, which is the time required for the gas bubbles to rise to the column top). The time step size was set such that the Courant- Friedrichs-Lewy Number (*CFL*) is lower than 1, as reported by Guédon et al. (2017). $\Delta t = 0.005$ s appeared as the optimal value.

The Phase Couple SIMPLE (PC-SIMPLE) algorithm was selected to handle the pressure–velocity coupling. A first-order Euler implicit scheme was used for temporal discretization. The Least Squares Cell Based formulation and the PRESTO! discretization methods were considered for spatial representation of gradients and pressure, respectively. In bubble columns, high order schemes are required to describe the transient nature of the flow, thus the QUICK method (third-order accurate) was implemented for both momentum and volume fraction equations. The First-Order Upwind was instead chosen for the turbulent quantities, because higher-order methods for turbulence and time discretization can drastically compromise numerical stability (Gemello et al. (2018a)). Concerning the *PBM* simulations, a First-Order Upwind scheme was selected for the discretization of the gas size bins. The solution methods are summarized in Table 1. A mass-flow inlet boundary condition was assigned at the sparger openings.

Concerning the *PBM* simulations, the inlet bubble size is assumed to have a log-normal distribution with a constant variance σ_b about the

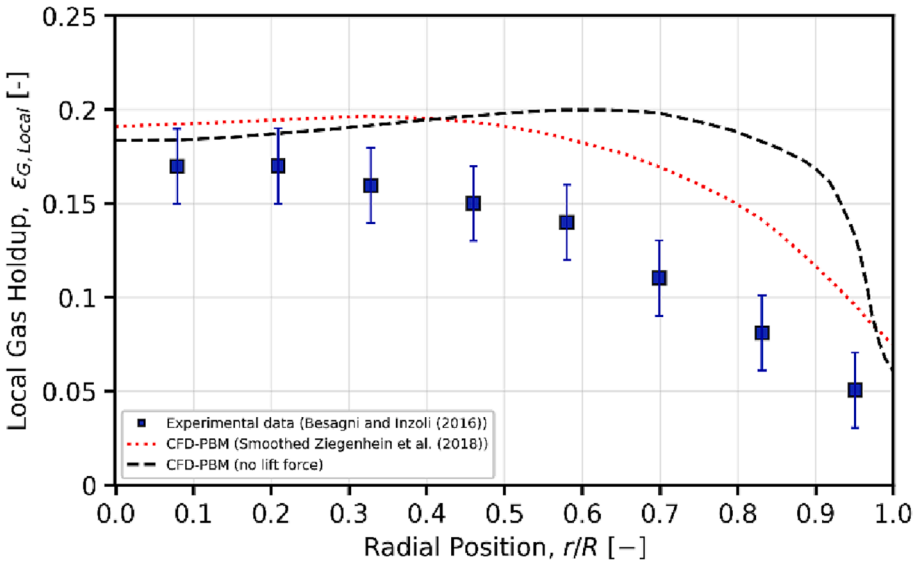

Fig. 19. Comparison of the *CFD* results for the radial profile of local gas holdup at the axial position of 0.7 m from the sparger at $U_G = 0.0614$ m/s using the *PBM* with lift force (dotted line) and the *PBM* without lift force (dashed line) versus the experimental data (■). Error bars represent the standard error of the experimental data.

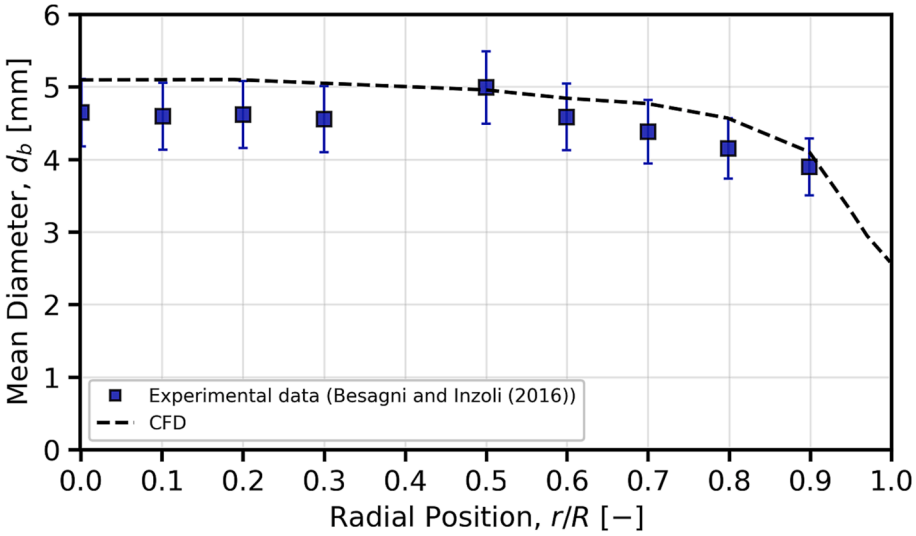

Fig. 20. Comparison of the *CFD* results for the radial profile of the *SMD* at the axial position of 0.7 m from the sparger at $U_G = 0.0188$ m/s using the *PBM* with lift force (dashed line) versus the experimental data (■). Error bars represent the standard error of the experimental data.

mean value μ_b. The inlet mean bubble size was calculated according to the Cao et al. (2009) correlation for the dimensionless bubble diameter $d_{b,w}$.

$$d_{b,w} = 1.7522 N_w^{0.362} \tag{28}$$

Where N_w is the dimensionless hole velocity, calculated considering the gas velocity at the sparger openings.

$$N_w = \frac{We}{(Fr)^{0.5}} \tag{29}$$

Given Equation (28) it is possible to determine the mean value of the distribution.

$$d_{b,w} = d_{b,\text{inlet}} \left(\frac{g\rho_L}{d_0 \sigma_L} \right)^{1/3} = \mu_b \left(\frac{g\rho_L}{d_0 \sigma_L} \right)^{1/3} \tag{30}$$

Where d_0 is the sparger openings diameter.

From the experimental data of Besagni and Inzoli (2016), the variance σ_b was set to 19%. It was assumed that the BSD produced by the sparger openings with the same hole diameter not depend on the sparger arm, otherwise 6 different distributions were required for each superficial gas velocity.

The inlet gas volume fraction was set to 1 and a no-slip boundary condition was applied at the walls. A pressure-outlet boundary condition was assigned at the top section of the column, and a complete backflow of gas was imposed.

The inlet turbulent quantities were defined following the correlations of Kawase and Moo-Young (1989) for the bulk liquid turbulent kinematic viscosity, $\bar{\nu}_t$, and the average mixing length, $\bar{l}$, in bubble columns.

$$\bar{\nu}_t = \frac{1}{33.9} g^{1/3} D_H^{4/3} U_G^{1/3} \tag{31}$$

$$\bar{l} = 0.1 D_H \tag{32}$$

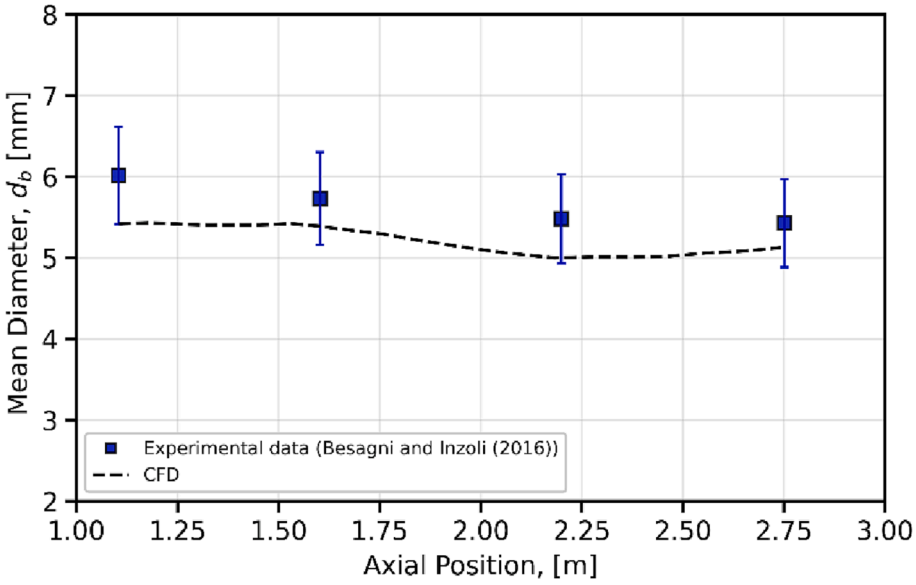

Fig. 21. Evolution of the *SMD* at different axial positions in the developed flow region of the column at $U_G = 0.0188$ m/s: (■) Experimental data of (Besagni and Inzoli, 2016), (dashed line) *CFD* results using swarm factor correction, *PBM* and lift force. Error bars represent the standard error of the experimental data.

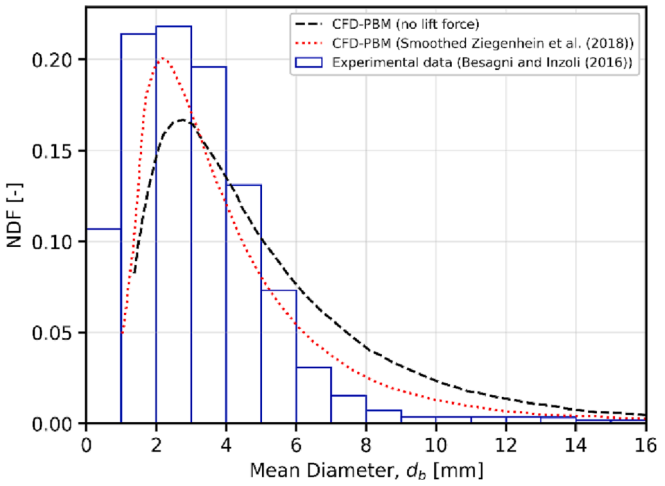

Fig. 22. Histogram representing the experimental BSD at $U_G = 0.0188$ m/s, compared with the BSD predicted by the *CFD* model adopting the *PBM* without the lift force (dashed line) and the lift force (dotted line).

The equations for the bulk liquid turbulent kinetic energy, $\overline{k}_L$, and bulk liquid turbulent dissipation rate, $\overline{\varepsilon}_L$, results:

$$\overline{k}_L = \left(\frac{\overline{v}_t}{\overline{l}C_\mu^{1/4}}\right)^2 \tag{32}$$

$$\overline{\varepsilon}_L = C_\mu^{3/4}\frac{\overline{k}_L^{3/2}}{\overline{l}} \tag{33}$$

Here, the factors $C_\mu^{1/4}$ and $C_\mu^{3/4}$ in the above equations ensure consistency with the definition of turbulent length scales for two-equation turbulent model. The bulk liquid turbulent specific dissipation rate, $\overline{\omega}_L$, is given as:

$$\overline{\omega}_L = \frac{\overline{k}_L}{\overline{l}C_\mu^{3/4}} \tag{34}$$

Equation 33 and Equation 35 were used to set the inlet and initial conditions of the liquid turbulence quantities. Due to the lack of information regarding turbulent quantities of the dispersed phase, they were set as liquid ones.

Lastly, to enhance stability the Bi-Conjugate Gradient Stabilized method (*BSGTAB*) was selected, and the number of pre-sweeps cycles were set to 1 in the multigrid options tab. To improve convergence rate, the Warped-Face Gradient Correction and the High-Order Term Relaxation options were also included.

3.7. Fluid properties

Both phases were considered incompressible, even if air is subject to a change in density along the column height due to the hydrostatic pressure variation. Water properties were taken at ambient pressure and temperature. Air properties were calculated at the midpoint of the column, where pressure is P = 1.16 bar. All values are listed in Table 2.

4. Results and discussion

Numerical results from CFD simulations are presented, discussed and compared to the experimental data. Results in terms of gas holdup, cross-sectional void fraction distribution, and cross-sectional liquid velocity distribution are analysed.

Firstly the mono-dispersed model, including only the drag force and the swarm factor ("*Swarm factor simulations*") is considered. Secondly, results given by the model including the PBM ("*PBM simulations*"), are discussed and compared with those provided by the swarm factor simulations. To conclude, the effect of the lift force on the numerical results is analysed by adding the smoothed Ziegenhein et al. (2018) lift force to the *PBM* simulations.

4.1. Swarm factor simulations

A first set of simulations was performed using a fixed bubble size, rounding the available experimental data for the mean bubble diameter. The drag model alone is not sufficient to capture the flow dynamics, and largely overestimated values were computed for the global gas holdup (with a relative error even greater than 100 % at high superficial gas

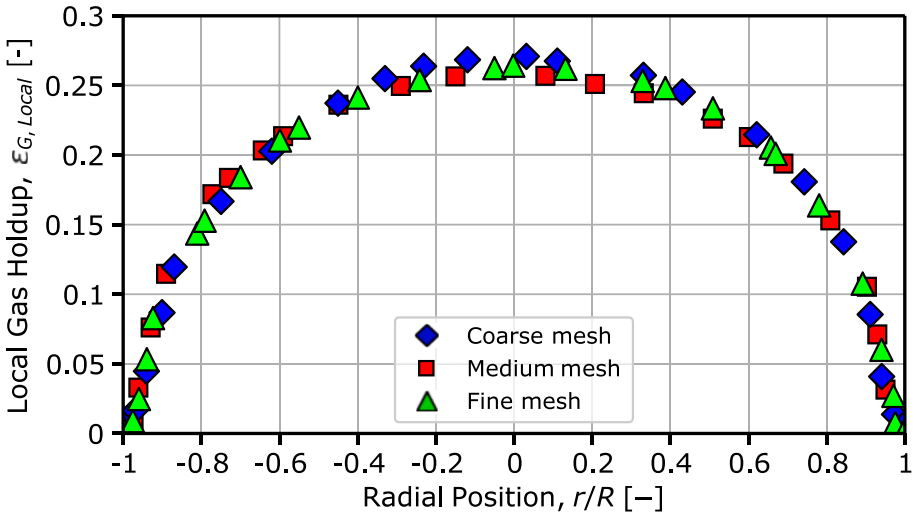

Fig. 23. Grid independence study on the local gas volume fraction profile at 1.9 m from the sparger at $U_G = 0.10$ m/s.

Table 4
Global gas holdup calculated with three grids at $U_G = 0.10$ m/s tested during the mesh independence analysis.

Mesh	Number of elements	Global Gas Holdup [%]
Coarse	230,000	17.58
Medium	313,000	17.2
Fine	436,000	17.2

velocity) (Fig. 10). Unacceptable results were also provided for the local gas volume fraction and axial liquid velocity. Consequently, the drag law was corrected with a swarm factor. It was followed the same approach reported in Gemello et al. (2018a), who modified the model of Simonnet et al. (2008) by adding a minimum constant value, h_{min} to which the factor must approach at high gas volume fractions. h_{min} is an adjustable parameter and must be tuned against experimental data, and thus can be different for different column configurations. After few tests, h_{min} was set to 0.40, resulting in pretty accurate predictions for the global gas holdup (Fig. 10), with a relative error always below the 10 % margin (Fig. 11), which is typically related to the error associated with the measurement method used to evaluate this quantity (Maximiano Raimundo (2015)).

Although the drag modification correctly determines the global flow properties, the local distribution of the gas holdup at low superficial gas velocity differs from the experimental profile. In the developed flow region, a parabolic profile was expected, but, instead, the numerical model calculates a flat distribution (Fig. 12a). At high superficial gas velocity, the model gives more realistic radial gas volume fraction profiles (Fig. 12b). The CFD results for the axial liquid velocity are in good agreement with the predictions calculated with the correlation of Forret et al. (2003) (Fig. 13). Moreover, the model is also able to track the behaviour of transient flow structures and large-scale liquid recirculation patterns, as shown in Fig. 14, where the instantaneous contour of the liquid velocity over the axial section of the column is represented. This representation is consistent with the experimental flow visualization (Chen et al. (1994)), and different flow regions can be noticed. In the near sparger region, the streamlines for the liquid velocity show a complex behaviour, with the formation of unstable flow structures that are then recovered when the flow reaches the fully developed condition at higher axial position. Also note the presence of vortices beneath the sparger level, which however seem not to affect the flow properties.

4.2. PBM simulations

Effect of the *CFD-PBM* coupled model are analysed and discuss in this section. The first parameter to take into consideration is the mean

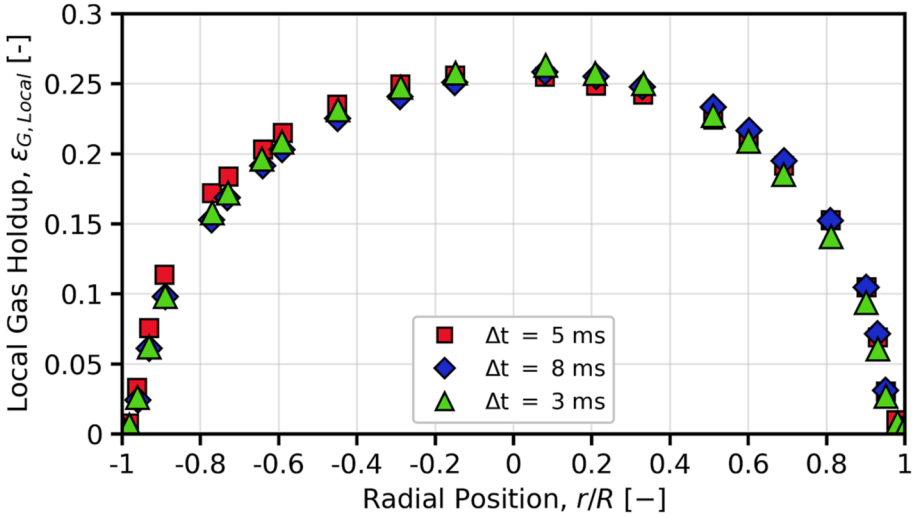

Fig. 24. Sensitivity analysis on the time step size. Effects on the local gas volume fraction profile at 1.9 m from the sparger and superficial gas velocity of 0.10 m/s.

bubble diameter, which is helpful in providing a screening of the quality of the numerical results. Considering a superficial gas velocity of 0.0188 m/s the outcomes of the simulation are in good agreement with the experimental findings. The volume-averaged experimental bubble mean diameter in the column was found to be 4.87 mm, while the CFD model reports a value of 4.68 mm (just a 3.9 % relative error). Additionally, since the class method tracks the Number Density Function (*NDF*) of the bubble population directly it is possible to evaluate the volume-averaged *NDF* given by the simulation: the overall distribution is reproduced with satisfactory accuracy (Fig. 15).

The predicted gas holdup is similar to the previous approach. At low superficial gas velocity, the discrepancies between experimental and numerical values remained almost unchanged (Table 3).

The effect of the *PBM* in the radial profile of the local gas holdup and axial liquid velocity is not particular relevant at low superficial gas velocity (Fig. 16). Some differences can be observed at high superficial gas velocity (Fig. 17), where the local void fraction profile predicted with the constant bubble size assumption appear to be slightly higher than those calculated with the *PBM*. This confirms that when an appropriate estimation of the mean bubble size is available (from experimental data), the *CFD* model can give fairly reliable results in the heterogeneous regime even if it is uses a single bubble size. It has to be noted that the model still predicts a flat holdup profile at low superficial gas velocity (Fig. 16): the *PBM* alone is not sufficient to reproduce the experimental the experimental shape of the local gas volume fraction profile, which results from the complex interactions and lateral movement of the bubbles, due to the strong poly-dispersity of the system.

4.3. The role of the lift force

CFD predictions for the radial profile of the local flow properties are reported in Fig. 18 and Fig. 19. The lift force allows to reproduce the parabolic shape in the local gas volume fraction profile, significantly improving the agreement with the experimental values. At very high superficial gas velocity the lift force has a lower impact compared to the previous cases at lower U_G (Fig. 18).

At low superficial gas velocities the flow regime is much more sensitive to the local flow instabilities caused by a non-uniform gas injection, for which bubbles with much higher diameter are produced by the larger holes located toward the end of each sparger arm. These local flow instabilities overcome the stabilizing effect of the turbulent dispersion and induce the peculiar parabolic shape of the local gas volume fraction. The model still struggles a little when dealing with the developing region of the flow just above the sparger. For example, consider the radial profile for the local gas holdup at 0.7 m from the distributor inlet (Fig. 19), the trend of the experimental points is well captured, but the simulation predicts larger gas fractions. In any case, the numerical results are improved with respect to the simple *CFD-PBM* coupled model without the lift force.

The use of the lift force generates a more physically sound gas volume fraction distribution. In particular, due to the bubble motion in the lateral direction, in the developed flow region a gradual increase in the gas volume fraction occurs from the column wall toward the axis. With only the swarm factor correction the local distribution of the gas volume fraction is much more uniform, resulting in a flat profile, as previously commented.

Including the lift force leads to better results also concerning the *BSD*. Considering $U_G = 0.0188$ m/s as an example, the radial profile of the bubble mean diameter matches very well with the experimental data near the sparger (Fig. 20) and the Sauter Mean Diameter is well predicted in the fully developed flow region (Fig. 21). In addition, results concerning the *NDF* of bubble size are improved with respect to the model neglecting the lift force (Fig. 22) since the lift force induces a lateral movement of the bubbles, enhancing the coalescence and breakup phenomena.

These considerations allow to complete a fully descriptive model that can represent adequately the hydrodynamics of a bubble column operated in the heterogeneous regime.

5. Conclusions

In this work, a *CFD* Eulerian-Eulerian model that could predict the complex flow evolution in a large-scale bubble column reactor operated with an air–water flow at high superficial gas velocity was presented and discussed. Specifically, numerical results concerning the global gas holdup and the local distribution of both gas volume fraction and axial liquid velocity were compared to the available experimental data at ambient conditions. The main conclusions can be summarized as following:

- The mono-dispersed approach that combines a drag law of Tomiyama (1998) with the swarm factor of Gemello et al. (2018a) can give reasonably accurate results with fairly low computational efforts if experimental data for the mean bubble size are available. A drawback of the proposed approach is that the parameter $h_{\min}$ must be corrected depending on the case under investigation.
- The screening of available coalescence and breakage models performed by Gemello et al. (2019) and Augier et al. (2021) allows to state that the set of kernels used in this work is the most suitable for bubble columns under the heterogeneous regime. The *CFD-PBM* coupled model predicts the Sauter Mean Diameter with good accuracy, but its influence of the radial profiles of the local flow properties is limited.
- The role of the lift force is critical when considering a highly non-uniform *BSD* generated at the sparger. In this case, bubbles experience a lateral motion, so that the large bubbles concentrate at the column centre, and the small bubbles are pushed toward the column walls. The Ziegenhein et al. (2018) modified lift coefficient correlation proposed in this study proved to be suitable for air–water systems, and numerical results that included the lift force modelling were found in very good agreement with the experimental data. At low superficial gas velocity, the correct parabolic shape for the gas holdup was obtained, whereas at high superficial gas velocity the effect of the lift force is lower, but it is still required to calculate more refined and accurate solutions.

Finally, some remarks and possible future developments are suggested:

- The modified swarm factor correlation proposed by Gemello et al. (2018a), as well as the breakage and coalesce expressions developed by Laakkonen et al. (2006) and Wang et al. (2005), depend on empirical parameter that are calibrated on experimental data. More effort has to be spent on developing theoretical models that are free from adjustable constants or, equivalently, to develop closed functionals expressions for these parameters.
- In depth study of the connection between the physical properties of the fluids and the local flow properties is still required to extend the use of this *CFD* model to industrial flows, that typically include organic solvents or additives and impurities (for example, ethanol).
- In this study, a constant gas pressure was used even though the change in the gas density from the bottom to the top of the column was not limited. Future studies should investigate the influence of the change in density of the gas phase on the numerical results.
- Other aspects not considered in this work may need more accurate investigation, such as the influence of Bubble Induced Turbulence (*BIT*).
- It is also recommended to expand the existing dataset of experimental values used in this work by including data regarding liquid velocity profiles, turbulence quantities and BSDs for the heterogeneous regime. This could be helpful to understand the role of many key parameters on the fluid dynamic behavior of the reactor.

Declaration of Competing Interest

The authors declare that they have no known competing financial interests or personal relationships that could have appeared to influence the work reported in this paper.

Data availability

Data will be made available on request.

Appendix A:. Mesh sensitivity analysis

A mesh independence analysis was performed to check the dependence of the results on the cell size. Three different unstructured polyhedral grids were obtained by varying the number of elements, in order to compere the results in terms of local gas volume fraction and global gas holdup. The column hydrodynamics is simulated on each mesh by considering only the drag law of Tomiyama et al. (1998) and the swarm factor of Gemello et al. (2018a). Predicted local gas holdup is very similar and the three profiles can be practically superimposed (Fig. 23). A slight deviation is observed for the coarse case when computing the global gas holdup (Table 4). Guédon et al. (2017) concluded that the mesh should be sufficiently fine to capture all flow structures and instabilities, hence the medium mesh was selected, representing the best trade-off between reasonable computational time and accuracy of the results.

Appendix B:. Time step sensitivity analysis

A time step size sensitivity analysis was performed, to check the independence of the numerical solution on the time step size. Two different time step sizes were tested, obtained by increasing and decreasing the optimal time step size ($\Delta t = 0.005$ s) by 60%. The column is simulated with the different time steps by the model including only the drag force of Tomiyama et al. (1998) and the swarm factor of Gemello et al. (2018a). Profiles of local gas volume fraction are then compared in Fig. 24: predicted results lay on the same curve and only small differences are visible in the left-side portion of the profile. This finding allows to conclude that the numerical solution is independent on the time step size if it is kept sufficiently low to avoid convergence issues.

References

Augier, F., Gilli, E., Maximiano Raimundo, P., 2021. One-equation model to assess population balance kernels in turbulent bubbly flows. Chem. Eng. Sci. 229, 116096.

Besagni, G., 2021a. The effect of operating and design parameter on bubble column performance: The LOPROX case study. Chin. J. Chem. Eng. 40, 48–52.

Besagni, G., 2021b. Bubble column fluid dynamics: A novel perspective for flow regimes and comprehensive experimental investigations. Int. J. Multiph. Flow 135.

Besagni, G., Inzoli, F., Ziegenhein, T., Lucas, D., 2017. Computational fluid-dynamic modeling of the pseudo-homogeneous flow regime in large-scale bubble columns. Chem. Eng. Sci. 160, 144–160.

Cao, C., Zhao, L., Xu, D., Geng, Q., Guo, Q., 2009. Investigation into bubble size distribution and transient evolution in the sparger region of gas - liquid external loop airlift reactors. Ind. Eng. Chem. Res. 48 (12), 5824–5832.

Chen, R.C., Reese, J., Fan, L.-S., 1994. Flow structure in a three-dimensional bubble column and three-phase fluidized bed. AIChE J. 40 (7), 1093–1104.

Clift, R., Grace, J., Weber, M., 1978. Bubbles, drops, and particles. Academic Press.

Colombo, M., Fairweather, M., 2015. Multiphase turbulence in bubbly flows: RANS simulations. Int. J. Multiph. Flow 77, 222–243.

Deen, N., 2001. An Experimental and Computational Study of Fluid Dynamics in Gas-Liquid Chemical Reactors. Aalborg University, Esbjerg, Denmark. PhD thesis,.

Degaleesan, S., Dudukovic, M., Pan, Y., 2001. Experimental study of gas-induced liquid-flow structures in bubble columns. AIChE J. 47 (9), 1913–1931.

Forret, A., Schweitzer, J.-M., Gauthier, T., Krishna, R., and Schweich, D. (2003). Influence of scale on the hydrodynamics of bubble column reactors: an experimental study in columns of 0.1, 0.4 and 1m diameters. Chemical Engineering Science, 58(3): 719 – 724. 17th International Symposium of Chemical Reaction Engineering (IS CRE 17).

Gemello, L., Cappello, V., Augier, F., Marchisio, D.L., Plais, C., 2018a. CFD-based scale-up of hydrodynamics and mixing in bubble columns. Chem. Eng. Res. Des. 136, 846–858.

Gemello, L., Plais, C., Augier, F., Cloupet, A., Marchisio, D., 2018b. Hydrodynamics and bubbe size in bubble columns: Effects of contaminants and spargers. Chem. Eng. Sci. 184, 93–102.

Gemello, L., Plais, C., Augier, F., Marchisio, D.L., 2019. Population balance modelling of bubble columns under the heterogeneous flow regime. Chem. Eng. J. 372, 590–604.

Gourich, B., Vial, C., Essadki, A.H., Allam, F., Soulami, M.B., Ziyad, M., 2006. Identification of flow regimes and transition points in a bubble column through analysis of differential pressure signal—influence of the coalescence behavior of the liquid phase. Chem. Eng. Process. 45 (3), 214–223.

Grace, J., Wairegi, T., Nguyen, T.H., 1976. Shapes and velocities of single drops and bubbles moving freely through immiscible liquids. Trans. Inst. Chem. Eng. 54, 167–173.

Guédon, G.R., Besagni, G., Inzoli, F., 2017. Prediction of gas–liquid flow in an annular gap bubble column using a bi-dispersed eulerian model. Chem. Eng. Sci. 161, 138–150.

Hosseini, A., Mereu, R., Canu, S., Zeigenhein, T., Lucas, D., Inzoli, F., 2020. Multiphase numerical modeling of a pilot-scale bubble column with a fixed poly-dispersity approach. Int. J. Multiph. Flow 128.

Ishii, M., Zuber, N., 1979. Drag coefficient and relative velocity in bubbly, droplet or particulate flows. AIChE J. 25 (5), 843–855.

Kawase, Y., Moo-Young, M., 1989. Turbulence intensity in bubble columns. Chem. Eng. J. 40 (1), 55–58.

Khan, I., Wang, M., Zhang, Y., Tian, W., Su, G., Qiu, S., 2020. Two-phase bubbly flow simulation using CFD method: A review of models for interfacial forces. Prog. Nucl. Energy 125.

Laakkonen, M., Alopaeus, V., Aittamaa, J., 2006. Validation of bubble breakage, coalescence and mass transfer models for gas–liquid dispersion in agitated vessel. Chem. Eng. Sci. 61 (1), 218–228.

Lehr, F., Millies, M., Mewes, D., 2002. Bubble-size distributions and flow fields in bubble columns. AIChE J. 48 (11), 2426–2443.

Liao, Y., Lucas, D., 2010. A literature review on mechanisms and models for the coalescence process of fluid particles. Chem. Eng. Sci. 65 (10), 2851–2864.

Maximiano Raimundo, P., 2015. Analysis and modelization of local hydrodynamics in bubble columns. Universit Grenoble A. PhD thesis,.

McClure, D.D., Norris, H., Kavanagh, J.M., Fletcher, D.F., Barton, G.W., 2014. Validation of a computationally efficient computational fluid dynamics (CFD) model for industrial bubble column bioreactors. Ind. Eng. Chem. Res. 53 (37), 14526–14543.

Petitti, M., Vanni, M., Marchisio, D.L., Buffo, A., Podenzani, F., 2013. Simulation of coalescence, break-up and mass transfer in a gas–liquid stirred tank with CQMOM. Chem. Eng. J. 228, 1182–1194.

Rollbusch, P., Bothe, M., Becker, M., Ludwig, M., Grünewald, M., Schlüter, M., Franke, R., 2015. Bubble columns operated under industrially relevant conditions – current understanding of design parameters. Chem. Eng. Sci. 126, 660–678.

Rzehak, R., Krauß, M., Kováts, P., Zähringer, K., 2017. Fluid dynamics in a bubble column: New experiments and simulations. Int. J. Multiph. Flow 89, 299–312.

Schiller, L., Naumann, N., 1935. A drag coefficient correlation. Vdi Zeitung 77, 318–321.

Shaikh, A., Al-Dahhan, M., 2007. A review on flow regime transition in bubble columns. Int. J. Chem. React. Eng. 5, 1–68.

Silva, M.K., d'Ávila, M.A., Mori, M., 2012. Study of the interfacial forces and turbulence models in a bubble column. Comput. Chem. Eng. 44, 34–44.

Simonnet, M., Gentric, C., Olmos, E., Midoux, N., 2008. CFD simulation of the flow field in a bubble column reactor: Importance of the drag force formulation to describe regime transitions. Chem. Eng. Process. 47 (9), 1726–1737.

Tabib, M.V., Roy, S.A., Joshi, J.B., 2008. CFD simulation of bubble column — an analysis of interphase forces and turbulence models. Chem. Eng. J. 139 (3), 589–614.

Tomiyama, A., 1998. Struggle with computational bubble dynamics. Multiph. Sci. Technol. 10 (4), 369–405.

Tomiyama, A., Tamai, H., Zun, I., Hosokawa, S., 2002. Transverse migration of single bubbles in simple shear flows. Chem. Eng. Sci. 57 (11), 1849–1858.

Wang, T., Wang, J., and Jin, Y. (2005). Theoretical prediction of flow regime transition in bubble columns by the population balance model. Chemical Engineering Science, 60(22):6199 – 6209. 7th International Conference on Gas-Liquid and Gas-Liquid-Solid Reactor Engineering.

Wellek, R.M., Agrawal, A.K., Skelland, A.H.P., 1966. Shape of liquid drops moving in liquid media. AIChE J. 12 (5), 854–862.

Wilkinson, P.M., Spek, A.P., van Dierendonck, L.L., 1992. Design parameters estimation for scale-up of high-pressure bubble columns. AIChE J. 38 (4), 544–554.

Zhang, D., Deen, N., Kuipers, J., 2006. Numerical simulation of the dynamic flow behavior in a bubble column: A study of closures for turbulence and interface forces. Chem. Eng. Sci. 61 (23), 7593–7608.
Ziegenhein, T., Lucas, D., 2019. The critical bubble diameter of the lift force in technical and environmental, buoyancy-driven bubbly flows. Int. J. Multiph. Flow 116, 26–38.
Ziegenhein, T., Rzehak, R., Krepper, E., Lucas, D., 2013. Numerical simulation of polydispersed flow in bubble columns with the inhomogeneous multi-size-group model. Chem. Ing. Tech. 2013 (85), 1080–1091.
Ziegenhein, T., Tomiyama, A., Lucas, D., 2018. A new measuring concept to determine the lift force for distorted bubbles in low Morton number system: Results for air/water. Int. J. Multiph. Flow 108, 11–24.